



ANIMAL LOCOMOTION

Mechanical intelligence simplifies control in terrestrial limbless locomotion

Tianyu Wang^{1,2,3†}, Christopher Pierce^{2,4†}, Velin Kojouharov³, Baxi Chong², Kelimar Diaz², Hang Lu⁴, Daniel I. Goldman^{1,2*}

Copyright © 2023 the Authors, some rights reserved; exclusive licensee American Association for the Advancement of Science. No claim to original U.S. Government Works

Limbless locomotors, from microscopic worms to macroscopic snakes, traverse complex, heterogeneous natural environments typically using undulatory body wave propagation. Theoretical and robophysical models typically emphasize body kinematics and active neural/electronic control. However, we contend that because such approaches often neglect the role of passive, mechanically controlled processes (those involving “mechanical intelligence”), they fail to reproduce the performance of even the simplest organisms. To uncover principles of how mechanical intelligence aids limbless locomotion in heterogeneous terradynamic regimes, here we conduct a comparative study of locomotion in a model of heterogeneous terrain (lattices of rigid posts). We used a model biological system, the highly studied nematode worm *Caenorhabditis elegans*, and a robophysical device whose bilateral actuator morphology models that of limbless organisms across scales. The robot’s kinematics quantitatively reproduced the performance of the nematodes with purely open-loop control; mechanical intelligence simplified control of obstacle navigation and exploitation by reducing the need for active sensing and feedback. An active behavior observed in *C. elegans*, undulatory wave reversal upon head collisions, robustified locomotion via exploitation of the systems’ mechanical intelligence. Our study provides insights into how neurally simple limbless organisms like nematodes can leverage mechanical intelligence via appropriately tuned bilateral actuation to locomote in complex environments. These principles likely apply to neurally more sophisticated organisms and also provide a design and control paradigm for limbless robots for applications like search and rescue and planetary exploration.

INTRODUCTION

Organisms from flapping hawkmoths (1) to prancing gazelles (2) to undulating snakes (3) and nematodes (4) produce directed movement through a combination of neural and mechanical control. Neural circuits integrate and process sensory information to produce locomotor commands through complex signaling networks. This helps organisms produce directed movement, despite the constantly changing external environment, by modulating motor commands in response to environmental cues. Much progress has been made in understanding the neural aspects of locomotor control, including the structure, function, and dynamics of neural circuits, particularly with genetic models such as *Caenorhabditis elegans* (5), *Drosophila melanogaster* (6), zebrafish (7), and mice (8).

In addition to purely neural control, “neuromechanical” approaches have been developed to describe the interaction between active neuronal controls and purely mechanical processes arising from body-environment interactions. This approach has been applied primarily to flying and walking systems (1, 9, 10). For example, fruit flies have been found to recover from flight disturbances through reflexive turning responses to mechanical stimuli (11), whereas running guineafowl have been shown to stabilize their gaits in rough terrain through passive adaptive responses (“preflexes”) mediated by the nonlinear properties of the musculature (12). In general, body-environment interactions can help coordinate the movements of the body through purely mechanical

control processes, a phenomenon known as mechanical or physical intelligence (13). A complete description of organismal locomotion must therefore place principles of neural/computational intelligence and mechanical intelligence on an equal footing, leading to the concept of embodied intelligence (14–16).

Although much attention has been paid to mechanical intelligence in legged and aerial systems, less is known about the interplay of neural and mechanical control in limbless locomotion. This locomotor strategy occurs within diverse and often highly complex, heterogeneous environments and spans length scales from meter-long snakes (17–19) with more than 10^8 neurons to the millimeter-long nematode worm *C. elegans* (Fig. 1A), which navigates complex microenvironments like rotting fruit (Fig. 1E and movie S1) with only 302 neurons (20, 21). Across the taxonomic and neuroanatomical diversity of lateral undulators, many organisms, including snakes and nematodes, use similar actuation mechanisms: bilaterally arranged bands of muscle that propagate waves of contralateral activation down the body, producing undulatory waves that lie in a plane (Fig. 1, A and C). The ubiquity and biological diversity of undulation, the continual environment-body hydro- and terradynamic interactions, and the existence of common mechanisms of actuation across organisms suggest an important role for mechanical intelligence in limbless locomotion.

Given the importance of mechanics and the challenges of modeling locomotor-environment interactions, using robots as “robophysical” models to identify key neuromechanical principles is appealing (22–24). These models incorporate simplified descriptions of organismal mechanics and neural control and thus can be used to elucidate the emergent “template-level” dynamics of organisms (25). This approach has been particularly successful in identifying the role of mechanical control in legged locomotion, including hopping (26), bipedal (27), quadrupedal (28), and hexapodal (29) locomotion and, later, flapping flight (30). These “terradynamic” systems have forced

¹Institute for Robotics and Intelligent Machines, Georgia Institute of Technology, 801 Atlantic Dr NW, Atlanta, GA 30332, USA. ²School of Physics, Georgia Institute of Technology, 837 State St NW, Atlanta, GA 30332, USA. ³George W. Woodruff School of Mechanical Engineering, Georgia Institute of Technology, 801 Ferst Dr NW, Atlanta, GA 30318, USA. ⁴School of Chemical and Biomolecular Engineering, Georgia Institute of Technology, 311 Ferst Dr, Atlanta, GA 30332, USA.

*Corresponding author. Email: daniel.goldman@physics.gatech.edu

†These authors contributed equally to this work.

researchers to confront the unpredictability, nonlinearity, and heterogeneity of the physical world. However, these concepts have been less extensively applied in modeling the complex terradynamic interactions and biomechanics of limbless locomotion.

Limbless robots, despite often being referred to as snake-like (31–34), have yet to match the locomotion capabilities of even the simplest limbless organisms like nematodes. Existing limbless robots, which often rely on complex and high-bandwidth sensing and feedback (35–37) are stymied by unpredictable terrain in the real world

that would not challenge their organismal counterparts (3, 20, 38). Beyond rigid systems, soft limbless robots with intrinsically compliant bodies have emerged over the last decade (39–41). However, control challenges that arise from air-/fluid-handling mechanisms and difficulties of modeling and modulating intrinsic material properties have limited their practical uses. Hence, limbless robots have yet to fulfill their promised potential for agile movement in the type of complex environments encountered in applications such as search and rescue and planetary exploration.

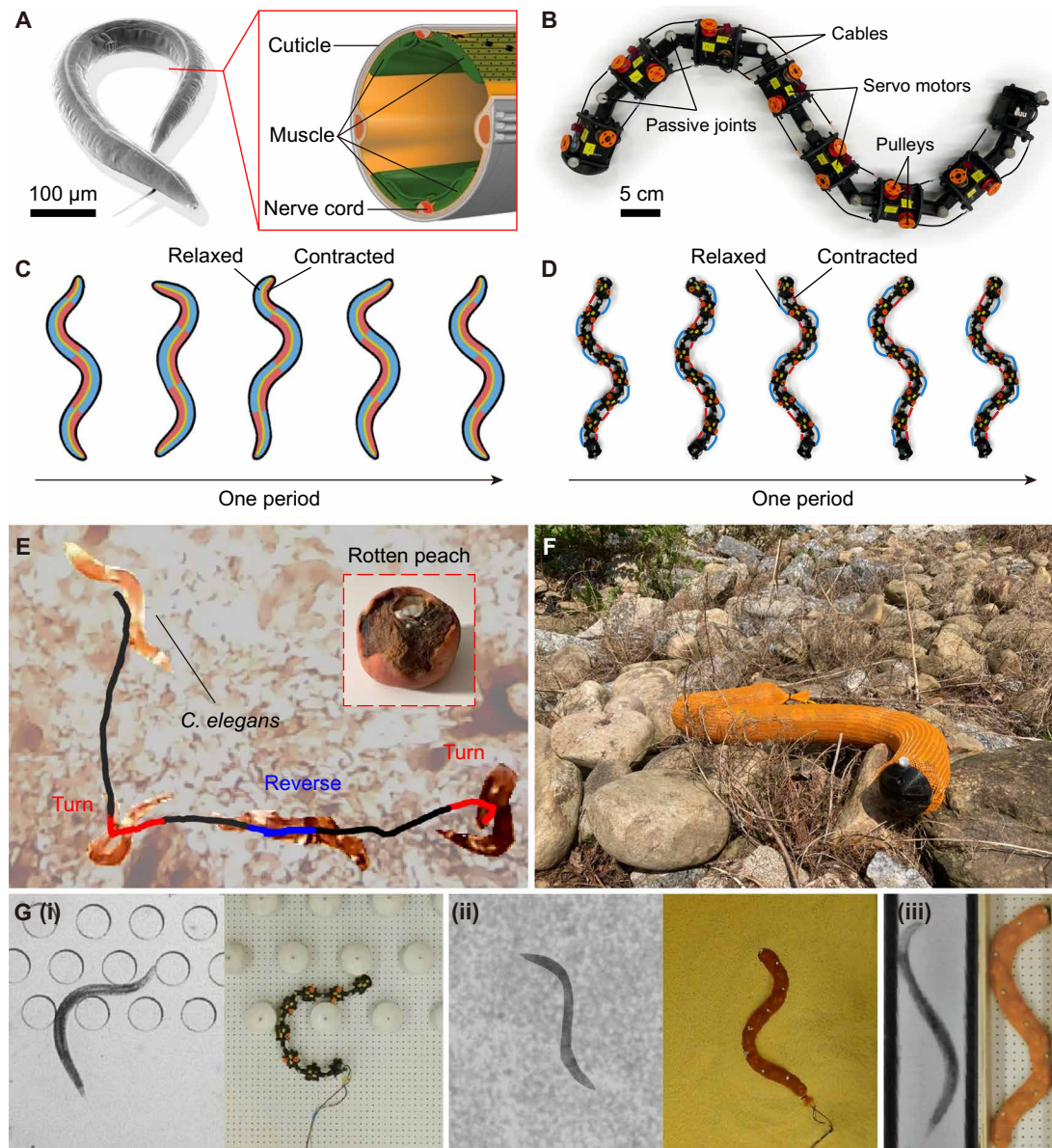


Fig. 1. Biological and robophysical limbless systems for understanding mechanical intelligence. (A) Nematode *C. elegans*, the biological model of this study (image credit: Ralf J. Sommer), along with a cross-sectional anatomy [reproduced from (97)] showing two pairs of bilaterally activated muscle bands. (B) Limbless robophysical model, implementing a bilaterally actuation mechanism. (C) Schematics of body postures and muscle activities over one gait period in the biological model. (D) Schematics of body postures and cable activities over one gait period in the robophysical model. (E) A nematode moves on a slice of rotten peach, a rheologically complex natural environment. (F) The robophysical model locomotes on a pile of rocks, a rheologically complex natural environment. (G) Biological and robophysical locomotion in comparable laboratory terrestrial environments: (i) lattices, (ii) granular media, and (iii) narrow channels.

One feature of elongated vertebrate and invertebrate organisms that is absent in the direct spinal actuation (joint actuation) design paradigm of limbless robots (31–34, 42–45) is bilateral actuation (Fig. 1C). Although simpler in design and control, the joint actuation mechanism limits the usefulness of limbless robotic models in identifying possible functional roles of bilateral actuation in mechanical control. Recent work has implied the importance of bilateral actuation in snakes (3) and limbless devices (46–48) when interacting with heterogeneities, suggesting that such an actuation scheme provides a degree of mechanical intelligence and thereby simplifies active control.

To advance our overall understanding and discover principles of mechanical intelligence in limbless locomotion and to understand the potential role of bilateral actuation specifically in mechanical control, we took a comparative biological and robophysical approach using two complementary models: a biological model, the nematode *C. elegans*, and a robophysical model, a limbless robot incorporating a bilateral actuation scheme that permits programmable, dynamic, and quantifiable body compliance (Fig. 1B). This compliance governs the passive body-environment interactions in the horizontal plane that allow mechanical intelligence. Because separating neural and mechanical aspects of control is challenging in a freely locomoting living system, we used the robot as a model (22, 24, 49, 50) that then allowed mechanical intelligence to be isolated from active controls and to be systematically tuned and tested.

Using comparisons between the kinematics and locomotor performance of our biological and robophysical models, we show that mechanical intelligence alone is sufficient for an open-loop limbless robot to reproduce locomotory behavior of nematodes. Mechanical intelligence simplifies controls in terrestrial limbless locomotion by taking advantage of passive body-environment interactions that enable heterogeneity negotiation, thereby stabilizing locomotion. Further, we show that a simple active behavior inspired by nematodes takes advantage of mechanical intelligence to enhance locomotion performance even further. Our method and results not only provide insight into the functional mechanism of mechanical intelligence in

organismal limbless locomotion but also provide an alternative paradigm for limbless robot development that simplifies control in complex environments.

RESULTS

Nematode kinematics and performance in heterogeneous terrains

C. elegans (Fig. 1A) has a fully mapped nervous system (5, 51) with a variety of available genetic tools for perturbing (52) and observing (53) neuromuscular dynamics. Compared with vertebrate undulators like snakes, its neural control architectures are simpler and better understood. Moreover, the limited information we have about its ecology and environment suggests that it is capable of contending with extremely varied and complex terrain like the interior of rotten fruit (20) (Fig. 1B). Hence, it is a promising model for understanding how neural feedback control and mechanical intelligence interact to generate limbless locomotion. We studied *C. elegans* locomotion kinematics using two-dimensional microfluidic hexagonal pillar arrays (hereafter referred to as lattices, where pillars are rigid and thus cannot move or deform upon collision with *C. elegans*) with varying pillar densities as model heterogeneous environments (Fig. 2A, i, v, and ix, and movie S1) (54, 55). These arrays capture aspects of the confinement and potential hindrance to locomotion that natural heterogeneity can impose. Unexpectedly, previous work has shown that rather than hindering locomotion, lattices can instead enhance nematode locomotor speeds (54, 55). Moreover, a previous numerical model of a nematode swimming in lattice implicated a strong role for passive mechanics in reproducing the behavior (55), suggesting that mechanical intelligence likely plays a role in nematodes' ability to take advantage of environmental interactions. However, the detailed kinematics of lattice traversal, particularly during inhibitory head collisions, have not been fully described.

To simplify the analysis of locomotion kinematics in lattices, we exploited dimensionality reduction techniques. Prior work applied principal components analysis to study undulating systems, such as

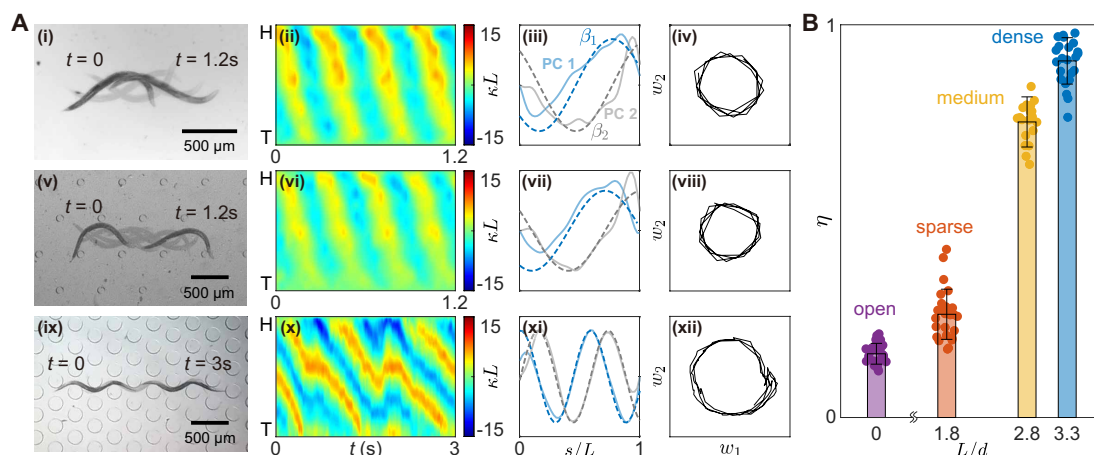


Fig. 2. Nematode kinematics and performance imply the role of mechanical intelligence. (A) Overlaid snapshots, effective body curvature, the first two dominant modes (solid lines are the principal components, and dashed lines are the best fits to sin and cos shape bases), and gait paths in the shape space of nematode locomotion in laboratory environments with varied pillar density. (B) Locomotion speed (wave efficiency η) as a function of obstacle density (measured as the ratio of body length and obstacle spacing L/d) for nematodes. Error bars represent SDs ($n = 26$ individuals in open and sparse lattices, $n = 20$ individuals in the medium lattice, and $n = 24$ individuals in the dense lattice).

nematodes and snakes, and illustrated that most body postures can be described by linear combinations of sine-like shape-basis functions, despite the inherently high dimensionality of postural data (56, 57). By considering the first two dominant principle components (Fig. 2A, iii, vii, and xi), we assumed that the body curvature profile κ at time t and location s ($s = 0$ denotes head and $s = 1$ denotes tail) can be approximated by

$$\begin{aligned}\kappa(s, t) &= w_1(t)\sin(2\pi\xi s + \phi) + w_2(t)\cos(2\pi\xi s + \phi) \\ &= w_1(t)\beta_1(s) + w_2(t)\beta_2(s)\end{aligned}\quad (1)$$

where ξ is the spatial frequency of body undulation obtained from direct fitting and ϕ is the emergent phase. $w_1(t)$ and $w_2(t)$ are the reduced shape variables describing the instantaneous shape of the locomotor at time t . Thus, by projecting curvatures onto the shape-basis functions $\beta_{1,2}(s)$ (Fig. 2A, iii, vii, and xi), the locomotion may be visualized as a path [the trajectory formed by $w_1(t)$ and $w_2(t)$] in a two-dimensional “shape space” defined by w_1 and w_2 (Fig. 2A, iv, viii, and xii; details are provided in Materials and Methods).

We studied nematode locomotion in four environments with varying pillar density, $L/d = 0$ (open fluid), 1.8 (sparse lattice), 2.8 (medium lattice), and 3.3 (dense lattice), where L represents nematode body length and d denotes pillar spacing. Consistent with previous observations (58), the nematodes performed an approximate traveling wave motion in homogeneous open fluid. In the shape space, this leads to circular orbits, where one full rotation corresponds to a single undulation cycle (Fig. 2A, i to iv). The nematode maintained a traveling wave-like gait in all lattice spacings, despite pitch differences. In sparser lattices (Fig. 2A, v to viii), the body kinematics were similar to those in a bulk fluid. Only in the dense lattice (Fig. 2A, ix to xii) did we observe deviations from an ideal traveling wave. However, these deviations were small and transient so that the overall path in shape space remained mostly circular. These deformations were typically correlated with body deformations induced by collisions (typically between the head and an obstacle) and rapidly (~ 0.4 s) returned to smooth traveling wave motion. Thus, environmental heterogeneities were observed to induce small perturbations that returned to a stable circular orbit, suggesting that the basic strategy of propagating traveling waves along the body is robust to intrusions by obstacles.

We further systematically evaluated nematode locomotor performance in terms of locomotion speed, measured by the wave efficiency η , the ratio of the forward center of mass speed to the wave propagation speed (Fig. 2B; refer to Materials and Methods for the detailed procedure for wave efficiency measurement). In free swimming, nematodes produced thrust because of the inherent drag anisotropy experienced in a viscous fluid (59); for the purposes of this paper, we define drag anisotropy as the ratio of the maximum forces on a small element translating through a continuous medium at angles perpendicular and parallel to the element's surface. We noticed that thrust-producing interactions with pillars produced larger η relative to the free swimming case (54, 55), despite the similarity of the kinematics. As pillar density was increased, by contrast, wave periodicity was frequently disrupted by inhibitory interactions (or, producing force opposite the direction of travel), typically coinciding with interactions between the nematode's head and a pillar. However, in the densest lattices, bouts of smooth traveling wave propagation between head interactions displayed an overall increase in η . In this regime, the nematode can take advantage of thrust-producing interactions with the lattice to increase η but avoids inhibitory collisions that would lead to jamming and getting

stuck. We hypothesized that the mechanism of stabilization is primarily passive in nature and that mechanical intelligence is sufficient for heterogeneity negotiation, without the need of explicit modulations of body postures.

Bilaterally actuated robophysical model development

To test whether mechanical intelligence alone is sufficient to reproduce the performance of nematode lattice traversal, we developed a hard-soft hybrid robophysical model (86 cm long with seven bending joints) that models the bilateral actuation scheme of nematodes and other limbless organisms, actuating joints by shortening and lengthening cables via decentralized cable-pulley-motor systems (each cable is independently controlled) on either side of each joint (Fig. 1D and movie S2). By properly coordinating the lengths of cables through waves of angular oscillation passing along the body, this robophysical model can produce similar undulatory locomotion as limbless organisms (Fig. 1, B and E). Although its movements are slower than those of limbless organisms, the highly damped nature of the locomotion in both systems (viscous in the nematodes, frictional in the robot) allows the robophysical model to offer insight into the function of mechanical intelligence in complex terrain navigation in the organism. Specifically, we introduce a nondimensional parameter, the “coasting number” \mathcal{C} , which can be viewed as the ratio of inertial to dissipative forces or as a characteristic timescale for a locomotor to come to rest from steady-state speed normalized by a cyclic timescale. For the robot, which is dominated by surface friction, $\mathcal{C} \sim 10^{-3}$, whereas nematodes are dominated by viscosity swimming in fluid and $\mathcal{C} \sim 10^{-2}$ (see Supplementary Discussion for calculations of \mathcal{C}). To compare the robophysical model and the organism, we assumed that they both exist in a regime in which resistive force theory (RFT) (60, 61) applies with frictional and viscous resistive forces, respectively. In this regime, the locomotor performance of a given gait is largely determined by the drag anisotropy and not the specific functional forms of the drag forces (for example, velocity-dependent/viscous versus velocity-independent/frictional). In our case, using passive, non-actuated wheels, we experimentally matched the drag anisotropy of the nematodes in the fluid by changing the wheel surface material (see Supplementary Methods), enabling us to achieve similar performance for nematodes in open fluid and robots locomoting on open, flat terrain.

The bilateral cable actuation mechanism enables body compliance in the robophysical model. However, in contrast to soft limbless robots that inherit compliance from soft materials that are usually hard to modulate, cables in our robophysical model are nonelastic, and thus, their lengths can be explicitly controlled. This allows the body compliance in our robophysical model to be quantifiable, programmable, inhomogeneous, and anisotropic, simply by appropriately coordinating the lengthening and shortening of cables. To implement a basic traveling wave locomotion pattern on the robophysical model as observed in nematodes, we developed the control scheme based on the “serpennoid” shape-based template (62). The template can generate a central pattern that enables a wave to propagate from head to tail if the i th joint angle α_i in the spine at time t follows

$$\begin{aligned}\alpha_i(t) &= A\sin\left(2\pi\xi\frac{i}{N} - 2\pi\omega t\right) \\ &= A\cos(2\pi\omega t)\sin\left(2\pi\xi\frac{i}{N}\right) - A\sin(2\pi\omega t)\cos\left(2\pi\xi\frac{i}{N}\right) \quad (2) \\ &= w_1(t)\beta_1^\alpha(i) + w_2(t)\beta_2^\alpha(i)\end{aligned}$$

where A , ξ , and ω are the amplitude and spatial and temporal frequencies of the wave; i is the joint index; and N is the total number of joints. The joint angle α given by this template will be further referred to as the “suggested” angle (the angle that would be realized absent all external and internal forces apart from those applied by the cables). Thus, the suggested gait path [the trajectory of $w_1(t)$ and $w_2(t)$] forms a perfect circle in the shape space spanned by w_1 and w_2 .

To implement programmable body compliance in the robophysical model, we developed a cable length control scheme based on the suggested angle template, where the lengths of the left and right cables (L_i^l and L_i^r) for the i th joint following

$$L_i^l(\alpha_i) = \begin{cases} \mathcal{L}_i^l(\alpha_i) & \text{if } \alpha_i \leq -(2G_i - 1)A \\ \mathcal{L}_i^l[-A \cdot \min(1, 2G_i - 1)] + l_0 \cdot [(2G_i - 1)A + \alpha_i] & \text{if } \alpha_i > -(2G_i - 1)A \end{cases}$$

$$L_i^r(\alpha_i) = \begin{cases} \mathcal{L}_i^r(\alpha_i) & \text{if } \alpha_i \geq (2G_i - 1)A \\ \mathcal{L}_i^r[A \cdot \min(1, 2G_i - 1)] + l_0 \cdot [(2G_i - 1)A - \alpha_i] & \text{if } \alpha_i < (2G_i - 1)A \end{cases} \quad (3)$$

where α_i is the suggested angle, A is the wave amplitude as in Eq. 2, and \mathcal{L}_i^l and \mathcal{L}_i^r are the exact lengths of left and right cables to form α_i . l_0 is a design parameter that determines how much a cable will be lengthened and is fixed throughout this work (see Supplementary Methods for more discussion). G_i is the generalized compliance for the i th joint, a key controller parameter to enable programmable body compliance. Specifically, in this work, we kept the generalized compliance value the same throughout all joints, $G_1 = \dots = G_N = G$. The generalized compliance $G \in [0, +\infty)$ is a parameter that expands the range of possible angles that can occur for a given suggested angle by altering the lengths of the cables on alternate sides; thus, G intuitively works as a standalone “knob” in the control that allows for programmable body compliance—increasing G leads to more compliance. Moreover, G is a dimensionless quantity that quantifies body compliance and is not related to the robophysical model’s geometry and characteristics of the environment that the robophysical model locomotes in.

To provide a better understanding of the generalized compliance G , we narrate the robophysical model’s compliant states under three representative generalized compliance values below. At $G = 0$, the robophysical model is bidirectionally noncompliant (Fig. 3A). All cables are shortened [$L_i^l(\alpha_i) = \mathcal{L}_i^l(\alpha_i)$ and $L_i^r(\alpha_i) = \mathcal{L}_i^r(\alpha_i)$] so that joints are non-compliant. Note that $\mathcal{L}_i^l(\alpha_i)$ and $\mathcal{L}_i^r(\alpha_i)$ are the exact lengths of the left and right cables that are stretched straight to form an angle α_i on the i th joint (see Supplementary Methods for the full deviation of \mathcal{L}_i^l and \mathcal{L}_i^r based on the robophysical

model geometry). When G is equal to 0, joint angles can precisely track the suggested angles. The projection of joint angle trajectories in the configuration space to the shape space (following the method given by Eq. 1) then is a perfect circular orbit. Specifically, at $G = 0$, the robophysical model behaves as a conventional rigid limbless robot; all joints can resist forces from either sides.

At $G = 0.5$, the robophysical model is directionally compliant (Fig. 3B). Either the left or right cable of a joint is lengthened (L_i^l or L_i^r departs from \mathcal{L}_i^l or \mathcal{L}_i^r) so that the joint is directionally (anisotropically) compliant; thus, it can admit forces to bend further but reject forces from the other side that would otherwise cause the bend to decrease. In the directionally compliant state, a joint is allowed to form an angle (the emergent angle ζ) with a larger absolute value than the suggested angle (α): When a joint is suggested to bend to the right ($\alpha > 0$), the left cable will be lengthened (with an amount of $l_0\alpha_i$) so that the joint can be bent further to the right direction; thus, its emergent angle ζ can be larger than the suggested angle α , $\zeta \geq \alpha$, and vice versa, the right cable will be lengthened when $\alpha < 0$ so that $\zeta \leq \alpha$. Note that when α equals 0, $L_i^l(0) = \mathcal{L}_i^l(0)$ and $L_i^r(0) = \mathcal{L}_i^r(0)$ so ζ equals 0. As a result, the projections of all feasible joint trajectories of ζ into the shape space yield a feasible region for gait paths to be perturbed by external forces, where the inner boundary is the “suggested” circular gait orbit.

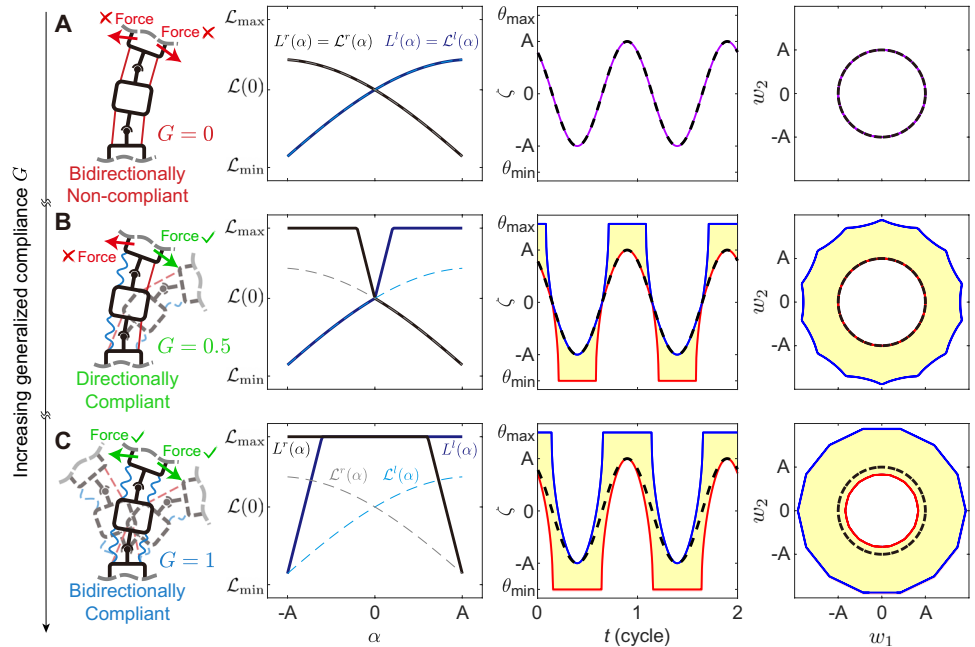


Fig. 3. Programmable and quantifiable body compliance in the robophysical model. Three representative compliant states of the robophysical model under varied generalized compliance G values: (A) bidirectionally noncompliant, (B) directionally compliant, and (C) bidirectionally compliant. The first column illustrates schematics of cable activation, where red cables are shortened and blue cables are lengthened. The second column shows how cables are lengthened at varied suggested angles according to the control scheme, where solid lines represent implemented cable lengths and dashed lines represent “exact” lengths of cables to form the suggested angle. The third column shows how much a feasible emergent angle ζ (yellow region) is allowed to deviate from the suggested angle α (dashed lines), where solid blue and red lines represent upper and lower boundaries of ζ , respectively. The last column shows how much a feasible emergent gait path in the shape space (yellow region) is allowed to deviate from the suggested circular gait path (dashed line), where solid blue and red lines represent outer and inner boundaries of feasible emergent gait paths, respectively.

At $G = 1$, the robophysical model is bidirectionally compliant (Fig. 3C). Both the left and right cables of a joint are lengthened (L_i^l and L_i^r depart from \mathcal{L}_i^l and \mathcal{L}_i^r) so that the joint is bidirectionally compliant; thus, it can admit forces from either side. In the bidirectionally compliant state, the emergent angle ζ of a joint can vary in both directions around α : At any given α , the left and right are both lengthened [with amounts of $l_0(A + \alpha)$ and $l_0(A - \alpha)$]. Note that when α equals A , $L_i^l(A) = \mathcal{L}_i^r(A)$ so ζ is greater than or equal to A , and similarly, when α equals $-A$, $L_i^l(-A) = \mathcal{L}_i^l(-A)$ so ζ is less than or equal to $-A$, meaning that the joint will only be directionally compliant when the suggested angle hits its maximum and minimum. In this state, the feasible region of the gait path in the shape space correspondingly expands as the inner boundary shrinks.

As a continuous quantity, when the generalized compliance value falls between representative values described above, the joint can exhibit a hybrid state. For example, when G is equal to 0.75, the joint will be bidirectionally compliant when α is an element of $(-0.5A, 0.5A)$ and will be directionally compliant otherwise. Further, as G value increases passing the bidirectionally compliant representative value, the cable constraints continue to loosen up, until G reaches a point where the joint becomes fully passive. Theoretically, the fully passive value is related to the robophysical model geometry and the gait parameter selection, whereas a consistent value of 1.75 is observed to correspond with full passivity throughout this work (the full derivation is provided in Supplementary Methods). To sum up, generalized compliance G works as a “knob” that we tuned to “program” how strongly the robophysical model is driven by the suggested shape, regulating the level of mechanical intelligence (movie S2). Thus, we varied G in the robophysical model to investigate at which level of body compliance its locomotor performance can approach nematodes. A full schematic of properties that the robophysical model displays under different G is shown in fig. S5.

Robophysical model kinematics and performance in heterogeneous terrains

To test the role of mechanical intelligence in limbless locomotion and its effect on locomotor performance, we conducted robophysical model experiments in four scaled-up environments (from open to dense) corresponding to the nematode study. Similar to the lattices for nematodes, pillars in the lattices for robophysical experiments cannot move and deform upon collision with the robophysical model. In each environment, the robophysical model was under open-loop control, executing a suggested traveling wave gait as in Eq. 2, with the shape parameters approximated directly from nematode kinematics in the corresponding environment so that the robophysical model used the same gaits as nematodes did (more specifically, the ratio of the body wavelength and the lattice spacing was kept the same between the robophysical model and nematodes; details of the approximation process are provided in Materials and Methods). We varied G to access the locomotion displayed by the robophysical model in each environment. Quantifying locomotor performance (the wave efficiency η , the ratio of forward center of mass speed to backward wave propagation speed) across the full range of G revealed that an appropriate G becomes necessary to facilitate open-loop traversal as heterogeneities arise (Fig. 4B). In flat terrain, η was inversely correlated to G . However, when obstacles were introduced, low G (≤ 0.5) resulted in frequent jams and became irreversibly stuck. At high G (≥ 1.5), the model failed to generate sufficient

self-propulsion. $G = 0.75$ emerges as an appropriate G value for locomotion in all heterogeneous environments, because local maxima of η display at $G \approx 0.75$ (movie S3). Further, η in the robophysical model with $G = 0.75$ increased as the obstacle density increased, well approaching η that displayed in nematodes (Fig. 4C).

To investigate the emergent robophysical model body kinematics, we tracked emergent joint angles ζ of the robophysical model, which are comparable to nematode emergent curvatures (detailed reasoning is provided in Supplementary Methods). We then projected ζ onto the shape-basis functions $\beta_{1,2}^\alpha$ to extract the shape space gait path formed by $w_1(t)$ and $w_2(t)$ as we did for nematodes. For $G = 0.75$ in the robophysical model, the body kinematics and gait orbits in the shape space (Fig. 4A) closely resembled those observed in nematodes (Fig. 2A). The model performed an approximate traveling wave motion in flat terrain and sparser lattices, which resulted in nearly circular orbits in the shape space. In the dense lattice, analogous to the nematodes, we also observed small deviations from ideal traveling wave shapes, which converged quickly back to the circular orbit. Thus, the robophysical model can serve as an effective model of nematode locomotion, capturing well both overall performance and detailed body kinematics (movie S4).

The emergent match between *C. elegans* and the robophysical model kinematics and the enhancement of performance at $G = 0.75$ compared with other G values resulted completely from body compliance—simply by programmatically and anisotropically loosening the physical constraints on the joints in a way that mirrors the geometry of organismal patterns of activity, which allows joints to passively deform under external forces. Such a seemingly counterintuitive result (improving performance via relaxing controls) verified our hypothesis that the appropriate level of mechanical intelligence (purely passively, mechanically controlled emergent body-environment interactions) can facilitate heterogeneity navigation and is sufficient to reproduce organismal lattice traversal performance.

Robophysical model force-deformation characterization

We used the force-deformation properties of the robophysical model to identify how interactions with obstacles lead to deformations to the suggested traveling wave kinematics that enable successful lattice traversal. By characterizing the relation between the external force F and the emergent joint angle ζ at suggested angles α , we achieved maps of force-deformation properties of the robophysical model with varied G values (Fig. 5; for other G values, see fig. S9). For low G , external forces produced minimal deformation of the joint for all parts of the cycle (unless they were sufficiently high to break the cable) (Fig. 5, A i and B ii). For high G , large deformations could be created in response to external forces in either direction (Fig. 5, A iii and B iii). However, at $G = 0.75$, force-deformation responses displayed a hybrid state (Fig. 5, A ii and B i): For small angles, force was admitted in both directions (bidirectionally compliant); for large angles, force was admitted in the direction of the bend but stiffly opposed in the opposite direction (directionally compliant).

We hypothesized that such hybrid compliance allows the selective exploitation of thrust-producing interactions through rigid responses and deformations that prevent jamming in detrimental interactions, such as head-on collisions. Our robophysical model and many other limbless undulators move through space by passing body waves from head to tail, with the wave velocity v_{wave} antiparallel to the center of mass velocity v_{CoM} (Fig. 6A). External forces F_{ext} from collisions that lie parallel to v_{wave} inhibit the center of mass motion, whereas collisions

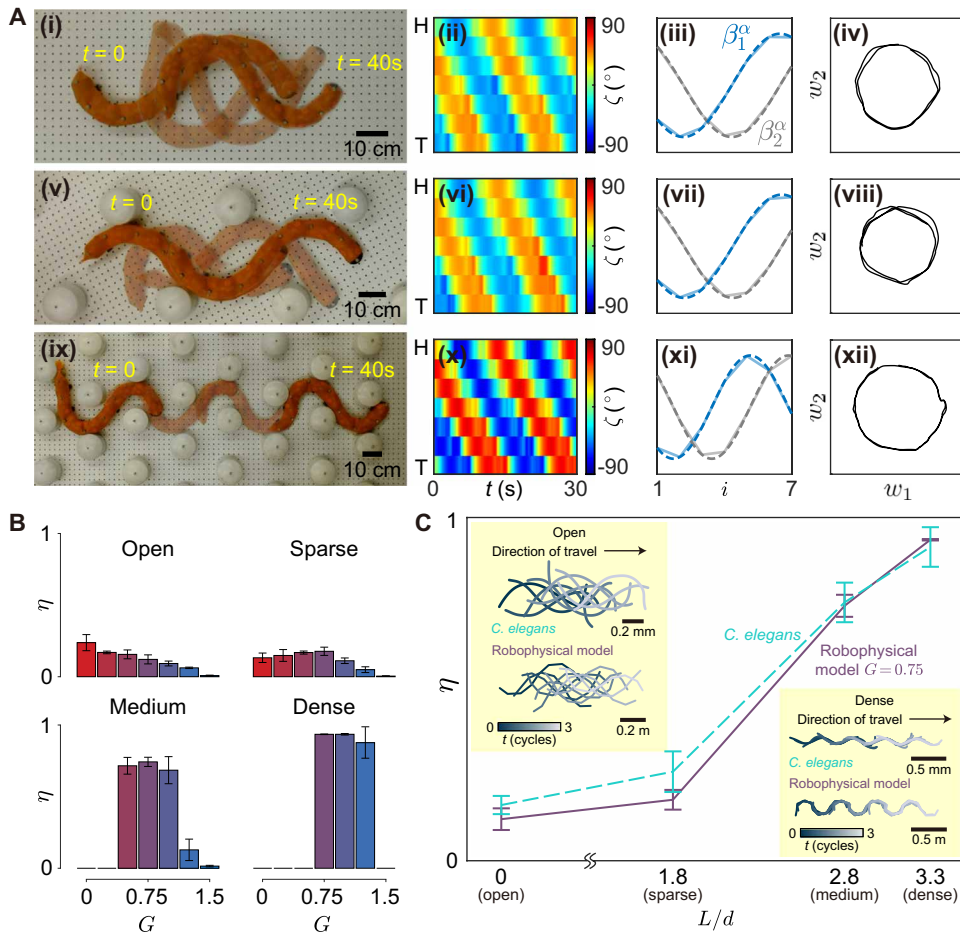


Fig. 4. Open-loop robot performance reveals the importance of mechanical intelligence. (A) Overlaid snapshots, emergent joint angles, shape basis, and gait paths in the shape space of robophysical locomotion ($G = 0.75$) in laboratory environments with varied obstacle densities. (B) Locomotion speed (wave efficiency η) of the robophysical model as a function of generalized compliance G in environments with varied obstacle densities (open, sparse, medium, and dense). Error bars represent the SD across three repetitions per experiment. (C) Comparison of locomotion speed as a function of obstacle density between the biological model *C. elegans* (reproduced from Fig. 2B) and the robophysical model with $G = 0.75$, accompanied by example time traces of splined points along the body as the nematode and the robophysical model move in the open and dense environments (insets). Error bars represent the SD across three repetitions per experiment.

that produce forces parallel to v_{CoM} produce thrust. Figure 6B shows the deflection from the suggested angle in response to a point force (≈ 3 N) parallel or antiparallel to v_{CoM} for a range of suggested joint angles at $G = 0.75$. At small suggested joint angles ($|\alpha| < 0.5A$), the joint displays a bidirectional compliant state, in which deflection is permitted more symmetrically ($F_{\text{ext}} \parallel v_{\text{CoM}}$ and $F_{\text{ext}} \parallel v_{\text{wave}}$) to produce a similar magnitude of deformation. However, as the suggested angle increases ($|\alpha| > 0.5A$), the joint becomes directionally compliant; such asymmetry produces an “easy” high-compliance axis and “hard” low-compliance axis. The direction of the easy and hard axes depends on the shape of the organism. When the “easy axis” is aligned with inhibitory interactions and the “hard axis” with thrust-producing interactions, organisms can resist buckling while maintaining forward progress. Figure 6C shows the orientation of the “easy”/high-compliance direction (black triangles) and the “hard” low-compliance (orange triangles) direction for three values of G (0, 0.75, and 1.5) and for the various joints along the body of an example eight-link undulator. Small arrows show point

forces acting along the body parallel to either v_{CoM} or v_{wave} . At $G = 0$, all joints are noncompliant; hence, point forces produce either jamming interactions (small red arrows) or thrust (green red arrows). At $G = 0.75$, the distribution of easy and hard axes is arranged such that would-be jamming interactions are converted into body deformations that lead to deflection and therefore successful obstacle traversal while still maintaining rigidity (noncompliance) in thrust-producing interactions. At $G = 1.5$, all interactions permit substantial deformations (all joints are highly bidirectionally compliant). Although jamming is avoided entirely, there is no ability to produce coherent thrust. Experimentally, the geometry of contacts closely follows the curvature profile of the gait (fig. S10). Would-be jamming interactions, for example, near the head, often lead to longer durations of contact, governed by the dynamics of the deformation under locally compliant joints, whereas thrust-producing interactions at higher curvature near the mid-body typically follow regular contact patterns with shorter duration contacts, matching the propagation of curvature along the body.

This simplified model (Fig. 6) revealed that for certain intermediate values of G , the robophysical model spontaneously converted inhibitory interactions into soft deflections while maintaining rigidity and thrust production in advantageous collisions without any explicit computation. Therefore, the coordinated shortening and lengthening of the cables served not only to realize an approximate traveling wave body shape sequence but also to dynamically modulate the compliance properties of the robot to buffer the motion to external collisions.

Emergent head behaviors in nematodes and the robophysical model

The robophysical model displayed emergent functional behaviors when G was equal to 0.75. Upon collision in the head, two typical head interaction events emerged in the robophysical model to exploit the asymmetric force-deformation response: “gliding,” where the head slides near-tangentially past the obstacle (Fig. 7A i), and “buckling,” where a collision induces a momentary increase in the local curvature near the head, which then facilitates a shallower angle of attack (Fig. 7A iii). Gliding led to only minor deviations from circular paths in the shape space (Fig. 7A ii), whereas buckling led to larger deviations from the circular orbit, because the radius of the path increased at a constant phase angle (Fig. 7A iv). This transient cessation of the wave phase velocity arose as the obstacle restricted the forward progress, constraining the body and inducing increased curvature. Among all of the events that we collected ($n \approx 100$), we classified 33.6% as buckling (with a phase pause over 0.5 s)

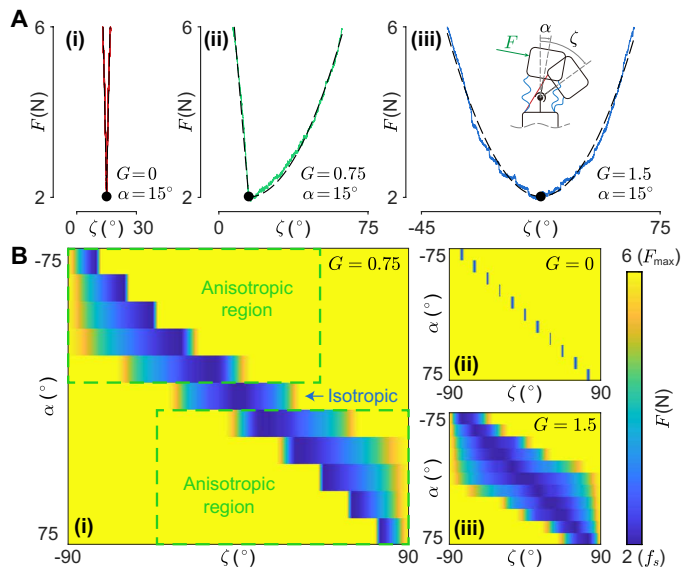


Fig. 5. Force-deformation characterization for the robophysical model. (A) External force versus emergent joint angle curves show behaviors of a joint reacting to external forces under different compliance states. **(B)** Force-deformation maps of the robophysical model with varied G values show that the robophysical model body compliance can be programmatically tuned.

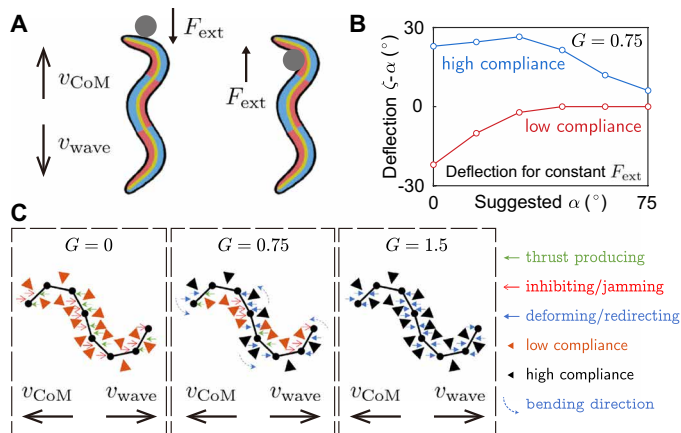


Fig. 6. A simplified model to understand the functional mechanism of mechanical intelligence. (A) Schematic illustration of an undulator facing inhibitory interactions (left) and thrust-producing interactions (right). **(B)** Deflection angle in response to a point force F_{ext} either parallel or antiparallel to v_{CoM} at $G = 0.75$ for different commanded angles, showing the response of the easy (high-compliance) direction and the hard (low-compliance) direction. **(C)** Geometry of easy (black triangles) and hard directions (orange triangles) for a single posture across three representative values of G . Small arrows show point forces that are thrust producing (green arrows), are jamming (red arrows), or result in deformation from the commanded shape (blue arrows), with bend directions indicated by the dashed blue lines.

and the other 66.4% as gliding. Given that such behaviors took place in the open-loop robophysical model only commanded with a suggested traveling retrograde wave, the gliding and buckling behaviors instigated by collisions occurred passively and therefore were dominantly determined by passive body-environment interactions.

Given the correspondence of gross locomotor performance and body kinematics of the robophysical model and *C. elegans* and the importance of head gliding and buckling dynamics in facilitating lattice transport, we next investigated whether *C. elegans* displayed similar head (or neck) dynamics during obstacle interactions. We observed substantially analogous behaviors (Fig. 7B, i to iv, and movie S5) such that 28.6% of head interaction events were classified as buckling (with a phase pause over 0.2 s), whereas the rest were considered gliding ($n \approx 100$). We thus posit that the nematodes' head interactions help to passively facilitate locomotion in heterogeneous environments as manifestations of mechanical intelligence. Specifically, potentially inhibitory collisions that might lead to jamming can be mitigated by asymmetrical compliance in the head.

Active reversals in nematodes and the robophysical model

Other than gliding and buckling head events, we also noted that in some instances *C. elegans* displayed a “reversal” behavior (Fig. 7B v) correlated with collisions that we did not see in the open-loop robophysical model. The reversal behavior is an actively controlled behavior (63), in which nematodes initiate a reversal of the direction of the traveling wave for a short period and then repropagate the original traveling wave (Fig. 7B vi). We hypothesized that active responses to heterogeneities (even as simple as reversals induced by head collisions) could benefit locomotion by augmenting mechanical intelligence. The active reversals induced by high angle of incident collisions supplement mechanical intelligence by providing an alternative means of modulating the angle of attack. This reversal behavior is likely initiated by mechanosensory neurons in the head, such as FLP (Fig. 7C), which have stereotyped anterior cellular processes that likely transduce mechanical inputs into signals that produce the reversals (64).

Similar to theoretical and computational models in biomechanics, robophysical models allow tests of hypotheses that are inconvenient with living systems. Thus, we next used the robophysical model to probe possible functional locomotor roles of the active reversal behaviors, positing that the inherent mechanical intelligence in the nematode could be augmented by simple head collision sensing feedback. To do so, we developed a head collision sensor (a force-sensitive resistor array; manufacturing and control details are given in Materials and Methods) for the model (Fig. 7C) to allow real-time collision angle and force estimation. To realize reversal behavior, we programmed the device to reverse the direction of wave propagation when a harsh head collision (large collision force and angle) was detected.

We studied the closed-loop robophysical model with reversal capability in the dense environment and compared its locomotor performance with open-loop results. Reversals enabled the robophysical model to traverse the environment in the low generalized compliance regime, which the open-loop strategy failed to traverse (Fig. 7D and movie S6), improving η in the range $0 \leq G \leq 0.5$. The reversal behaviors robustified the locomotion by increasing the range of G that allows the model to effectively locomote in the most challenging environment. The closed-loop robophysical model also showed substantially similar kinematics as observed in nematodes (Fig. 7A, v and vi, and Fig. 7B, v and vi, and movie S5). Robophysical experiments revealed the function of reversal behaviors in undulatory locomotors: By not simply repeating the same movement back and forth in place, reversals allow the locomotor to take advantage of mechanically intelligent dynamics, passively adjusting body postures

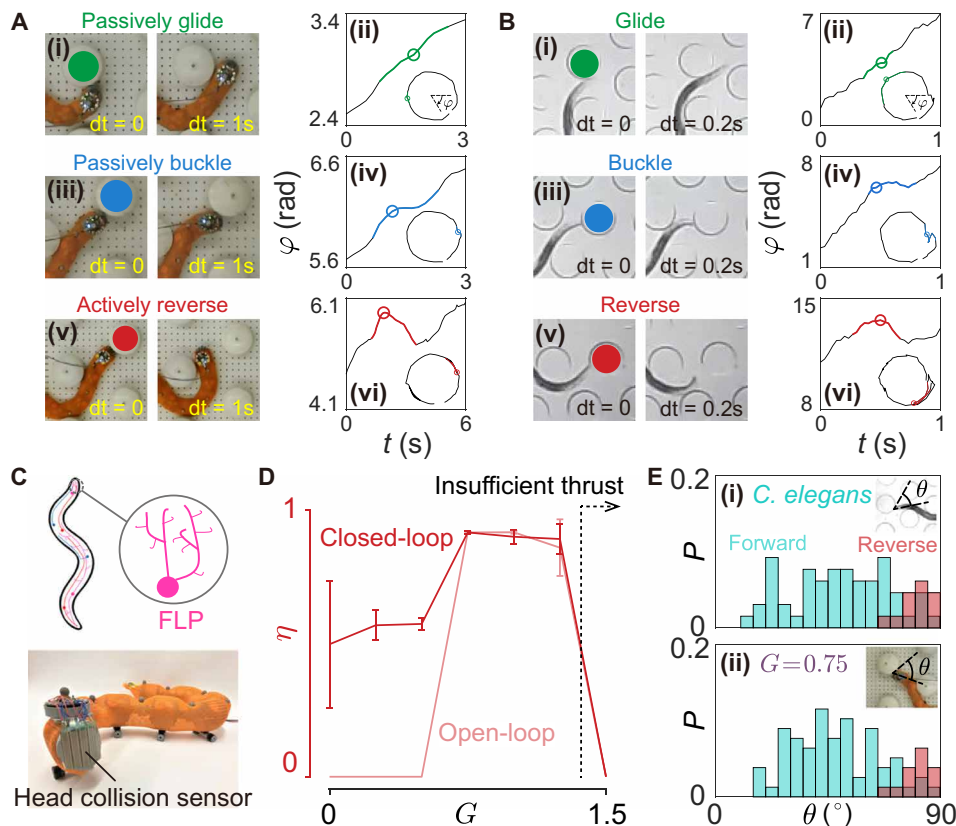


Fig. 7. Mechanical intelligence enables passive behaviors and can be augmented actively. (A) Passive gliding and buckling behaviors, and an active reversing behavior in the robophysical model, along with their corresponding characteristic phase-time plots. (B) Analogous behaviors displayed by the biological model, along with corresponding phase-time plots. (C) FLP dendrite sensory structure in nematodes and the head collision sensor in the robophysical model for studying how reversals augment mechanical intelligence. (D) Wave efficiency as a function of G in the dense environment for the robophysical model with and without reversals, showing that reversals can robustify robophysical locomotion. Error bars represent SDs across three repetitive trials of each experiment. (E) Head collision angle probability distributions classified by postcollision motion directions (forward or reverse) in nematodes and the closed-loop robophysical model ($G = 0.75$).

and spontaneously finding favorable positions and orientations to generate effective thrust for locomoting further.

Given the similarity in behavioral kinematics between the closed-loop robophysical model and nematodes, we further investigated head collision angles and corresponding postcollision movement directions (forward or reverse) in both systems. The probability distributions of head collision angle for forward and reverse motion further demonstrate that the reversal-capable robophysical model with $G = 0.75$ can capture well emergent behaviors that are induced by mechanical intelligence in *C. elegans* (Fig. 7E; probability distributions for other G values are shown in fig. S7) and thus works as a reliable model of *C. elegans* locomotion (an example comparison of body kinematics is shown in fig. S8; also note that this result applies to the presented robophysical model design and controls, given that the robophysical model's reversal behavior can be altered by a different head sensor implementation). Such qualitative agreement in body kinematics and the quantitative agreement in body event statistics imply that simple computational intelligence (reversals triggered by head sensing feedback) can compensate for a lack of mechanical intelligence (especially at the low- G region) or enhance mechanical intelligence (in terms of introducing extra chances for passive body-environment interactions) and thus

can augment locomotor performance. This also provides insight into the functional mechanism of the seemingly inefficient reversal behaviors displayed in nematodes. Our results also suggest that the spatiotemporal responses of the head sensory neurons such as FLP (65) may be tuned to help facilitate obstacle navigation. For instance, the spatial structure of the cellular processes within the head (Fig. 7C) may allow the nematode to sense the collision angle, explaining the angular dependence of the different collision behaviors (Fig. 7E). Further, the robophysical model demonstrates a comprehensive example of embodied intelligence (14, 16) and morphological computation (66, 67), displaying the most robust locomotion capabilities while working under the synergies of mechanical intelligence and computational intelligence.

Open-loop robot capabilities in laboratory complex environments

Nematodes do not only perform well in heterogeneous, collision-dominated environments. They also encounter a diverse array of substrates, including Newtonian fluids of varying viscosity and other flowable substances with complex, non-Newtonian rheologies (20). Hence, body compliance that enables lattice traversal may also improve performance in less-structured environments or, at a minimum, not disrupt performance. Therefore, we hypothesized that our bilaterally actuated limbless robophysical model would also display good performance without

major changes in control in a diversity of robophysical model terrains with properties similar to those encountered during search and rescue and other applications (Fig. 1G). We found that beyond functioning as a model for discovering and understanding emergent principles in limbless locomotion that cannot be directly tested with organisms, the bilaterally actuated limbless robot displayed substantial terrestrial mobility in diverse, complex, and more challenging environments.

We tested the robot in a range of laboratory and outdoor environments (Fig. 8, fig. S11, and movies S7 and S8). Beyond regular lattices, the robot demonstrated effective traversal in randomly distributed obstacle terrains (fig. S11A) and agile transitions from open terrain to obstacle terrain (fig. S11B), where the robot was under open-loop controls with $G = 0.75$. Without the need for active adaptation of body shapes (36, 68, 69) or selection of paths (70–72) based on the awareness of internal states (such as instantaneous joint angles or torques) or knowledge of the surrounding environment (for example, via contact sensing or visual feedback) as proposed in previous works, the mechanical intelligence in this robot enabled compliant body-environment interactions, facilitating the spontaneous locomotion.

Further, we conducted tests of locomotion speeds and cost of transport in other types of environment, first granular media (fig. S11C), a

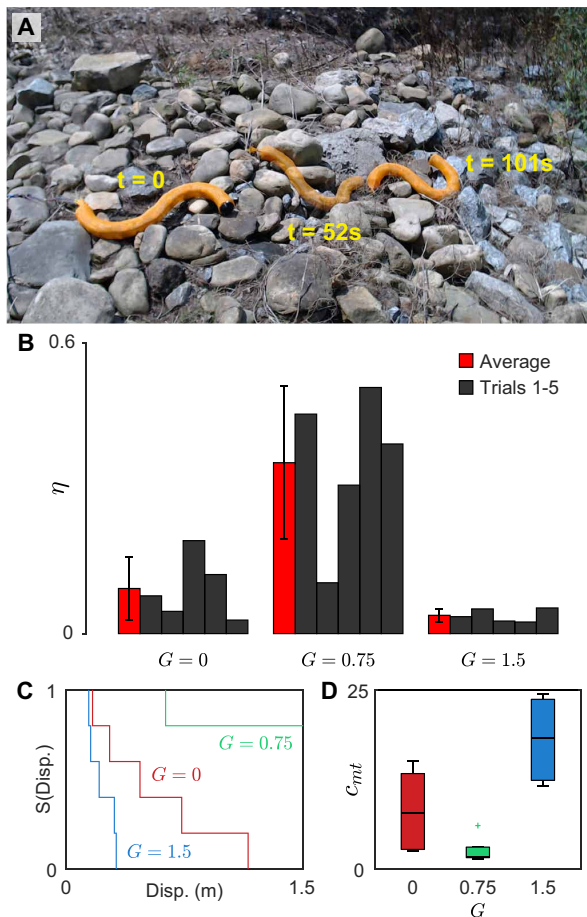


Fig. 8. Open-loop robot capabilities in real-world complex environments.

(A) Time-lapse photos of the open-loop robot traversing over a tightly packed rock pile with an intermediate generalized compliance value ($G = 0.75$). (B) Comparison of locomotion speeds (wave efficiency η) with varied G values on the rock pile. Error bars represent SDs. (C) The survivor function for varied G values with respect to displacement, measuring the robot's traveling distance before getting stuck or failing in motors. (D) Mechanical cost of transport (C_{mt}) for varied G on the rock pile, measuring the robot's energy efficiency of locomotion. Box central marks indicate the median; edges indicate the 25th and 75th percentiles. The whiskers cover data points within a range of 1.5 times the interquartile range, whereas outliers outside of this range are marked with a + symbol.

model flowable medium previously studied using other limbless systems (73, 74). In the granular material, we found that introducing an appropriate amount of passive body mechanics (by increasing G) can substantially reduce energy consumption without a notable loss of locomotor speed, with the local minimum in the cost of transport emerging at intermediate values of G (fig. S12).

We also tested the robot in narrow channels that functioned as models of pipes (fig. S11D), where we reversed the direction of the wave propagation to enable forward locomotion on the robot without wheels relying purely on wall interactions (see Supplementary Discussion). The generalized compliance G enables spontaneous shape adaptation/modulation to a highly constrained channel without the need to probe the channel width in advance. Further, the local minimum of cost of transport emerged at high compliance, $G = 1.25$. We also measured cost of transport in lattices with varied

obstacle densities (sparse, medium, and dense, as discussed previously), where we found that local maxima of locomotion speed and local minima of cost of transport all emerged at intermediate values of G . More detailed robot performance results and further discussions are included in Supplementary Discussion.

Open-loop robot capabilities in natural complex environments

To determine the potential benefits of mechanical intelligence in practical limbless robot applications and the generalizability of principles derived from two-dimensional laboratory environments to complex three-dimensional natural environments, we conducted open-loop locomotion experiments in a mechanically complex environment. Specifically, we tested the robot's performance in a randomly distributed and tightly packed pile of rocks (Fig. 8A and movie S8), simulating the terradynamic challenges that a limbless robot may face during search-and-rescue or planetary exploration tasks. Our quantitative analysis of robot locomotion performance demonstrated that, with an appropriate amount of generalized compliance ($G = 0.75$), mechanical intelligence facilitates effective negotiation with irregularities, ensuring successful locomotion. Conversely, inadequate compliance ($G = 0$) hindered obstacle traversal, whereas excessive compliance ($G = 1.5$) resulted in insufficient thrust generation (Fig. 8, B and C). Notably, the cost of transport exhibited local minima at intermediate values of G , consistent with our findings from laboratory tests (Fig. 8D).

Overall, laboratory and outdoor tests demonstrated that intermediate values of G enable effective locomotion in the largest range of environments and provide reduced costs of transport. This suggests that mechanical intelligence not only facilitates obstacle negotiation but also can improve locomotion speed and efficiency.

DISCUSSION

In summary, our integrative and comparative study of biological and robophysical limbless locomotors reveals that mechanical intelligence, the general collection of emergent adaptive behaviors that arise from passive body-environment interactions, simplifies control in terrestrial limbless locomotion, especially in heterogeneous environments, and is sufficient to reproduce organismal lattice traversal performance. The robophysical model, once programmed with an appropriate level of compliance, accurately models undulatory organisms not only in terms of locomotor performance and body kinematics but also in terms of dynamic force-deformation relationships [similar force-deformation relationships have been established for vertebrate undulators (75)]. Dynamic force-deformation relationships are non-trivial for an organism of the scale of *C. elegans* [only passive viscoelastic properties have been determined for *C. elegans* (76)]. Thus, our robophysical model is a useful tool for understanding the functional mechanism of mechanical intelligence in the organism: By identifying and understanding the mechanically intelligent control regimes of the robophysical model that accurately reproduce *C. elegans* kinematics in lattices, we can generate hypotheses about what underlying physiological and anatomical details are required to produce the emergent effective locomotion. Broadly, model organisms like *C. elegans* have an important role to play in connecting neural dynamics to behavior. Our results suggest that mechanics also play a substantial role in shaping behavior via processes that occur outside the nervous system and therefore must be understood and accounted for to reach a comprehensive understanding of animal behavior in general.

Robotic limbless locomotion in confined environments presents challenges in generating adequate thrust and preventing jamming caused by obstacles. Prior research has confronted this challenge through gait design and online parameter tuning approaches (32, 36, 37, 74). Essentially, if provided with sufficient foreknowledge of the environment or precise real-time proprioceptive sensory feedback (such as visual or internal body forces), it is possible that an “optimal” gait template can be carefully designed or “optimal” parameters within a template can be tuned online so that even a noncompliant robot can move effectively. In the case of lattices, optimal gaits will have wavelengths, amplitudes, and phasing that allow geometric conformity to the lattice (in other words, the wavelength and lateral displacement, determined by the amplitude, will be an integer multiple of the lattice spacing). However, developing and implementing such controllers and sensing modalities requires considerable effort and computational resources. Our approach of exploiting mechanical intelligence can replace these complicated processes, enabling the robot to move in complex environments with open-loop controls, using a simple traveling wave template with low sensitivity to the chosen wave parameters (so that slightly mismatched parameters do not fail to produce locomotion because of mechanical modulation of commanded shapes). Further, we verified in laboratory and natural complex environments that mechanical intelligence (in the form of the appropriate compliant actuation scheme) can even improve locomotion speed and efficiency. For nematodes, who rely on mechanical and chemical cues to navigate, gait selection based on foreknowledge of the environment is not possible; hence, the mechanical control scheme is likely important in traversing dense terrain. Even in organisms with vision, like snakes, the speed of locomotion often makes gait planning ineffective, and passive mechanisms again become substantial (3). Moreover, our results hint at mechanisms that govern the trade-off between active neural controls and passive body mechanics in nematodes. Our comparative exploration of mechanical intelligence could potentially offer a perspective that complements existing approaches to the question of the general role of neural versus mechanical control (55, 77–80).

Further, our demonstration of the advantages arising from our implementation of mechanical intelligence through the bilateral actuation mechanism presents several promising research avenues. Because we observed in experiments that the performance of the robophysical model operating at a certain G value can vary in different environments, we posit that developing a full mechanistic model of the dynamics of the system in various environments could further help determine “optimal” G values based on terrain properties. Because G can be dynamically tuned, we posit that adding sensory capabilities could enable the robot to learn or select the “optimal” G value in real time that accommodates best the current environment. Because each joint is controlled in a decentralized manner, we posit that locally varying G based on local sensing feedback would enable the system to maximize the utility of the surrounding environment to generate thrust and thus to locomote more effectively.

Finally, the bilateral actuation scheme suggests a design and control paradigm for limbless robots. Contrasting the lack of mechanical intelligence in limbless robots to date, the bilateral actuation mechanism offloads complex sensorimotor controls for handling body-environment interactions to mechanical intelligence, improving locomotion efficiency and freeing up onboard hardware and computational bandwidth for advanced sensing and motion planning techniques (37, 45, 70, 81–87). This represents a paradigm shift in limbless

robotics that could pave the way for the future development of more agile, intelligent, and capable limbless robots that fulfill their promised potential of maneuverability in extremely complex environments, finding diverse applications such as search and rescue, industrial inspection, agricultural management, and planetary exploration.

MATERIALS AND METHODS

Biological experiments and data processing

Wild-type *C. elegans* (QLN2) was used for all experiments. Nematodes were cultured using standard protocols on NGM agar plates with *Escherichia coli* (OP-50) lawns. Nematodes were cultured at 20°C and synchronized to day 1 adults for all studies.

Sequences of body curvatures over time of nematode locomotion in lattice were extracted from video recordings (details of lattice manufacturing and body curvature extraction are provided in Supplementary Methods). To simplify the analysis of locomotion kinematics in lattices, we exploited dimensionality reduction techniques. Prior work illustrated that most body postures in undulating systems can be described by linear combinations of sine-like shape-basis functions, despite the inherently high dimensionality of postural data (56, 57). We assume that the essence of the body curvature profile κ at time t and location s ($s = 0$ denotes head and $s = 1$ denotes tail) can be approximated by Eq. 1, where ξ is the spatial frequency of body undulation obtained from direct fitting. $w_1(t)$ and $w_2(t)$ are the reduced shape variables describing the instantaneous shape of the locomotor at time t . Thus, the locomotion may be visualized as a path through a two-dimensional “shape space” defined by w_1 and w_2 . Practically, we first performed principal components analysis to the curvature data $[\kappa(s, t)]$ to extract the first two principal components, which account for more than 90% of the variation in observed body configurations (fig. S2). Then, we fitted two shape-basis functions, in the form of $\sin(2\pi\xi s + \phi)$ and $\cos(2\pi\xi s + \phi)$, to the principal components (examples shown in Fig. 2A, iii, vii, and xi, where $\xi = 0.81, 0.80$, and 1.75 for presented examples, respectively). We projected the curvatures onto the shape-basis functions, by finding the least-squares solution (88), to extract the weights of shape-basis functions and reduced shape variables $w_1(t)$ and $w_2(t)$. The gait path then is the trajectory formed by $w_1(t)$ and $w_2(t)$ in the shape space spanned by w_1 and w_2 .

Collision events with pillars were identified manually, and the angle of the head and the pillar were calculated manually in ImageJ. To calculate wave efficiencies, bouts of locomotion containing at least three cycles of forward movement were selected. The wave efficiency was calculated as $\eta = v_{\text{CoM}}/v_{\text{wave}}$, where v_{CoM} is the center of mass velocity of the organism and v_{wave} is the wave speed. v_{CoM} was calculated directly from microscopy videos using the distance traveled by the nematode's head over an integer number of wave cycles. The wave speed $v_{\text{wave}} = f\lambda$ was calculated using the measured frequency and wavelength of each nematode. For the head collision angle of nematodes, we measured the angle between the body centerline and the tangential line of the pillar that passes the contact point. To classify gliding and buckling in the collection of head collision events that followed with forward body movement (no reversal), we examined the nematode body kinematics and calculated phase over time around the collision time. We classified the events that led to a phase pause over 0.2 s as buckling and others as gliding.

Robophysical experiments

We built laboratory models of heterogeneous terrains (fig. S1B) scaled to the dimensions of the robot, comparable to those used in

biological experiments. The wheels coated by low-friction fiberglass tape that were equipped on the robophysical model can create a $\sim 1.6:1$ drag anisotropy, which is close to that for nematode in the liquid between pillars, assumed to be modeled by a cylindrical cross section in a low Reynolds number viscous fluid (59, 61). Note that the magnitude of reaction force on wheels of the robophysical model is speed independent (89), whereas the magnitude of reaction force is linearly dependent on speed for nematodes in viscous fluid. However, drag anisotropy is the dominant factor in governing performance in undulatory locomotion (90), and the difference between frictional and viscous drag is likely to be subtle.

Finally, given that nematodes displayed different gaits in lattices with different densities, the robophysical model's suggested gait must be selected to replicate the kinematics of nematode locomotion. In each corresponding environment, we kept the ratio of the wavelength displayed on the body and the spacing of pillars in the lattice the same between the robophysical model and nematodes. This ensures that the robophysical model and the nematodes have similar periodic contacts with the lattice (fig. S10). As described previously, we tracked the centerlines of the nematode body in video recordings and approximated the wavelength of the nematode posture in each frame. We then averaged the wavelengths for all the frames and divided them by the pillar spacing of the lattice, yielding the wavelength-spacing ratio (~ 2 for the sparse environment, ~ 2.2 for the medium environment, and ~ 1.8 for the dense environment). On the robophysical model, we tuned the amplitude A and spatial frequency ξ in the suggested gait in Eq. 2 so that the robophysical wavelength-spacing ratio matched with nematode in each scaled-up environment. Specifically, in this work, we used $A = 46^\circ, 48^\circ, 51^\circ$, and 72° and $\xi = 0.82, 0.80, 0.58$, and 1.02 for open, sparse, medium, and dense environments, respectively. However, note that the choices of these parameters depend on the robophysical model's dimensional specifications, such as module length and the maximum range of joint bending.

The robophysical experiments were conducted on a level pegboard (Home Depot) measuring 2.4 m in length and 1.2 m in width, with 6.35-mm holes spaced every 25.4 mm. Each hole has screw inserts that are fitted for 4-mm bolts that can be used to secure PVC pipe caps. The pipe caps (Charlotte, 12.7 cm in diameter and 10 cm in height) were used as reconfigurable obstacles in the experiments. They have 4-mm holes drilled at their center and could be secured to the pegboard using long 4-mm bolts (McMaster-Carr) that were fastened into the screw inserts. An example lattice configuration is shown in fig. S1B. This experimental setup allows for obstacles to be easily rearranged and spaced on the pegboard to match the pillar spacings of different lattices in the nematode experiments.

The OptiTrack motion-tracking system was used to record the positions and postures of the robophysical model in the workspace. Six IR cameras (OptiTrack Flex 3) were mounted above the lattice to capture the real-time 3D positions of nine reflective markers attached to the robophysical model's body, including seven at each joint, one at the anterior end, and one at the posterior end. The X , Y , and Z position values of each marker were obtained from the Motive software using MATLAB. In addition, a high-resolution camera (Logitech HD Pro Webcam C920) was mounted above the experiment environment to record videos of each experiment. The footage was used to analyze the head collision angle probability distributions classified by postcollision motion directions.

Robophysical experiment protocol and data analysis

Robophysical experiments consisted of a series of trials running the robophysical model in the lattices. One trial was running the

robophysical model from an initial position until it reached one of the following states: (i) the robophysical model exited the lattice; (ii) the robophysical model got stuck (did not proceed for 10 consecutive gait cycles); or (iii) any of the servo motors overloaded (experiencing torque that exceeded the stall torque). Three separate trials were conducted for each generalized compliance value (ranging from 0 to 1.5 with a 0.25 interval) in each of the four environments (open, sparse, medium, and dense). To ensure consistency across trials, three initial positions were randomly selected and kept identical for all values of generalized compliance.

For the analysis of the robophysical model kinematics, we extracted emergent joint angles ζ using tracked positions of the markers. Given that we view the joint angles in the discretized body as equivalent to the curvatures in the continuous body, similar to nematodes, we projected ζ (that can vary with G) onto the suggested shape-basis functions $\beta_{1,2}^\alpha$ (that remain the same for all G values in a specific lattice setup) as in Eq. 2 by finding the least-squares solution. This allowed us to extract the reduced shape variables $w_1(t)$ and $w_2(t)$ and to analyze the robophysical model's emergent gait paths in the shape space. The methods for the calculation of wave efficiency and the measurement of head collision angle in the robophysical model were the same as nematodes, based on tracked data. The method for classification of the passive behaviors was the same as well, whereas the threshold of phase pauses for buckling classification was 0.5 s for the robophysical model.

Force-deformation characterization experiment

Force-deformation experiments were performed by measuring the relation between the magnitude of an external pushing force exerted on a joint with a certain G and the emergent joint angle. We designed and 3D-printed a stick to push the robophysical model. The stick was attached to a load cell (FUTEK LLB350-FSH03999), and the load cell was mounted on a robot arm (DENSO VS-087), as shown in fig. S9A. The robot arm was programmed to move the stick in a circular trajectory at a constant velocity of 1 mm/s, where the center of the circle was colinear with the rotation axis of the joint and the radius of the circle was 60 mm such that the pushing point was at the middle of the module. Analog signals of the load cell were passed through an analog amplifier (FUTEK IAA100) and then an analog-to-digital multifunctional data acquisition module (NI USB-6009), and the digital signal was recorded using NI LabVIEW. The robot body was fixed to a rigid table using two wooden planks that were firmly secured to the table. The robot was pinched between the planks, fixing it to the table surface. One single robot joint was left extending out past the planks for the force-deformation experiments. The joint was given a specified joint angle and G value before the start of the experiment. Specified angle values were swept from -75° to 75° with an increment of 15° .

In each experiment, the end effector of the robot arm began rotating in the clockwise direction from the suggested angle until the force reached a maximum value, set as 6 N, which was sufficiently large to bend a compliant joint but would not break the robophysical model. This process was repeated in the counter-clockwise direction starting from the suggested angle. Taking all force-emergent angle characterizations together, we show maps of force-deformation properties with varied G values (fig. S9B).

Supplementary Materials

This PDF file includes:

Supplementary Methods
Supplementary Discussion
Figs. S1 to S12
References (92–98)

Other Supplementary Material for this manuscript includes the following:

Movies S1 to S8
MDAR Reproducibility Checklist

REFERENCES AND NOTES

- J. Gau, R. Gemileire, L. V. (FM subteam), J. Lynch, N. Gravish, S. Sponberg, Rapid frequency modulation in a resonant system: Aerial perturbation recovery in hawkmoths. *Proc. Biol. Sci.* **288**, 20210352 (2021).
- R. M. Alexander, *Principles of Animal Locomotion* (Princeton Univ. Press, 2002).
- P. E. Schiebel, J. M. Rieser, A. M. Hubbard, L. Chen, D. Z. Rocklin, D. I. Goldman, Mechanical diffraction reveals the role of passive dynamics in a slithering snake. *Proc. Natl. Acad. Sci. U.S.A.* **116**, 4798–4803 (2019).
- C. Fang-Yen, M. Wyart, J. Xie, R. Kawai, T. Kodger, S. Chen, Q. Wen, A. D. T. Samuel, Biomechanical analysis of gait adaptation in the nematode *Caenorhabditis elegans*. *Proc. Natl. Acad. Sci. U. S. A.* **107**, 20323–20328 (2010).
- J. G. White, E. Southgate, J. N. Thomson, S. Brenner, The structure of the nervous system of the nematode *Caenorhabditis elegans*. *Philos. Trans. R. Soc. Lond. B Biol. Sci.* **314**, 1–340 (1986).
- A.-S. Chiang, C. Y. Lin, C. C. Chuang, H. M. Chang, C. H. Hsieh, C. W. Yeh, C. T. Shih, J. J. Wu, G. T. Wang, Y. C. Chen, C. C. Wu, G. Y. Chen, Y. T. Ching, P. C. Lee, C. Y. Lin, H. H. Lin, C. C. Wu, H. W. Hsu, Y. A. Huang, J. Y. Chen, H. J. Chiang, C. F. Lu, R. F. Ni, C. Y. Yeh, J. K. Hwang, Three-dimensional reconstruction of brain-wide wiring networks in *Drosophila* at single-cell resolution. *Curr. Biol.* **21**, 1–11 (2011).
- E. A. Naumann, J. E. Fitzgerald, T. W. Dunn, J. Rihel, H. Sompolsky, F. Engert, From whole-brain data to functional circuit models: The zebrafish optomotor response. *Cell* **167**, 947–960.e20 (2016).
- S. W. Oh, J. A. Harris, L. Ng, B. Winslow, N. Cain, S. Mihalas, Q. Wang, C. Lau, L. Kuan, A. M. Henry, M. T. Mortrud, B. Ouellette, T. N. Nguyen, S. A. Sorensen, C. R. Slaughterbeck, W. Wakeman, Y. Li, D. Feng, A. Ho, E. Nicholas, K. E. Hirokawa, P. Bohn, K. M. Joines, H. Peng, M. J. Hawrylycz, J. W. Phillips, J. G. Hohmann, P. Wahnoutka, C. R. Gerfen, C. Koch, A. Bernard, C. Dang, A. R. Jones, H. Zeng, A mesoscale connectome of the mouse brain. *Nature* **508**, 207–214 (2014).
- S. Sponberg, R. Full, Neuromechanical response of musculo-skeletal structures in cockroaches during rapid running on rough terrain. *J. Exp. Biol.* **211**, 433–446 (2008).
- M. A. Winter, *Biomechanics and Motor Control of Human Movement* (John Wiley & Sons, 2009).
- L. Ristroph, A. J. Bergou, G. Ristroph, K. Coumes, G. J. Berman, J. Guckenheimer, Z. J. Wang, I. Cohen, Discovering the flight autostabilizer of fruit flies by inducing aerial stumbles. *Proc. Natl. Acad. Sci. U. S. A.* **107**, 4820–4824 (2010).
- M. A. Daley, J. R. Usherwood, G. Felix, A. A. Biewener, Running over rough terrain: Guinea fowl maintain dynamic stability despite a large unexpected change in substrate height. *J. Exp. Biol.* **209**, 171–187 (2006).
- M. Sitti, Physical intelligence as a new paradigm. *Extreme Mech. Lett.* **46**, 101340 (2021).
- R. Pfeifer, M. Lungarella, F. Iida, Self-organization, embodiment, and biologically inspired robotics. *Science* **318**, 1088–1093 (2007).
- R. Pfeifer, J. Bongard, *How the Body Shapes the Way We Think: A New View of Intelligence* (MIT Press, 2006).
- F. Iida, G. Giardina, On the timescales of embodied intelligence for autonomous adaptive systems. *Annu. Rev. Control Robot. Auton. Syst.* **6**, 95–122 (2023).
- R. Gaymer, New method of locomotion in limbless terrestrial vertebrates. *Nature* **234**, 150–151 (1971).
- B. C. Jayne, Kinematics of terrestrial snake locomotion. *Copeia* **1986**, 915–927 (1986).
- Z. Guo, L. Mahadevan, Limbless undulatory propulsion on land. *Proc. Natl. Acad. Sci. U.S.A.* **105**, 3179–3184 (2008).
- M.-A. Félix, C. Braendle, The natural history of *Caenorhabditis elegans*. *Curr. Biol.* **20**, R965–R969 (2010).
- N. Cohen, J. H. Boyle, Swimming at low Reynolds number: A beginners guide to undulatory locomotion. *Contemp. Phys.* **51**, 103–123 (2010).
- N. Gravish, G. V. Lauder, Robotics-inspired biology. *J. Exp. Biol.* **221**, jeb138438 (2018).
- A. J. Ijspeert, Biorobotics: Using robots to emulate and investigate agile locomotion. *Science* **346**, 196–203 (2014).
- J. Aguilar, T. Zhang, F. Qian, M. Kingsbury, B. McInroe, N. Mazouchova, C. Li, R. Maladen, C. Gong, M. Travers, R. L. Hatton, H. Choset, P. B. Umbanhowar, D. I. Goldman, A review on locomotion robophysics: The study of movement at the intersection of robotics, soft matter and dynamical systems. *Rep. Prog. Phys.* **79**, 110001 (2016).
- R. Full, D. Koditschek, Templates and anchors: Neuromechanical hypotheses of legged locomotion on land. *J. Exp. Biol.* **202**, 3325–3332 (1999).
- F. Meyer, A. Spröwitz, L. Berthouze, Passive compliance for a rc servo-controlled bouncing robot. *Adv. Robot.* **20**, 953–961 (2006).
- S. Collins, A. Ruina, R. Tedrake, M. Wisse, Efficient bipedal robots based on passive-dynamic walkers. *Science* **307**, 1082–1085 (2005).
- G. Bledt, M. J. Powell, B. Katz, J. D. Carlo, P. M. Wensing, S. Kim, MIT Cheetah 3: Design and control of a robust, dynamic quadruped robot, in *2018 IEEE/RSJ International Conference on Intelligent Robots and Systems (IROS)* (IEEE, 2018), pp. 2245–2252.
- R. Altendorfer, N. Moore, H. Komsuolu, M. Buehler, H. B. Brown Jr, D. McMordie, U. Saranli, R. Full, D. E. Koditschek, Rhex: A biologically inspired hexapod runner. *Auton. Robots* **11**, 207–213 (2001).
- M. H. Dickinson, F.-O. Lehmann, S. P. Sane, Wing rotation and the aerodynamic basis of insect flight. *Science* **284**, 1954–1960 (1999).
- S. Hirose, M. Mori, Biologically inspired snake-like robots, in *2004 IEEE International Conference on Robotics and Biomimetics* (IEEE, 2004), pp. 1–7.
- A. A. Traneth, R. I. Leine, C. Glocker, K. Y. Pettersen, P. Liljebäck, Snake robot obstacle-aided locomotion: Modeling, simulations, and experiments. *IEEE Trans. Robot.* **24**, 88–104 (2008).
- A. Crespi, A. J. Ijspeert, Online optimization of swimming and crawling in an amphibious snake robot. *IEEE Trans. Robot.* **24**, 75–87 (2008).
- C. Wright, A. Johnson, A. Peck, Z. M. Cord, A. Naaktgeboren, P. Gianfortoni, M. Gonzalez-Rivero, R. Hatton, H. Choset, Design of a modular snake robot, in *2007 IEEE/RSJ International Conference on Intelligent Robots and Systems* (IEEE, 2007), pp. 2609–2614.
- J. Liu, Y. Tong, J. Liu, Review of snake robots in constrained environments. *Rob. Auton. Syst.* **141**, 103785 (2021).
- T. Wang, J. Whitman, M. Travers, H. Choset, Directional compliance in obstacle-aided navigation for snake robots, in *2020 American Control Conference (ACC)* (IEEE, 2020), pp. 2458–2463.
- F. Sanfilippo, J. Azpiazu, G. Marafioti, A. Traneth, Ø. Staudahl, P. Liljebäck, Perception-driven obstacle-aided locomotion for snake robots: The state of the art, challenges and possibilities. *Appl. Sci.* **7**, 336 (2017).
- T. Kano, T. Sato, R. Kobayashi, A. Ishiguro, Local reflexive mechanisms essential for snakes' scaffold-based locomotion. *Bioinspir. Biomim.* **7**, 046008 (2012).
- M. Luo, M. Agheli, C. D. Onal, Theoretical modeling and experimental analysis of a pressure-operated soft robotic snake. *Soft Robot.* **1**, 136–146 (2014).
- C. Branyan, C. Fleming, J. Remaley, A. Kothari, K. Tumer, R. L. Hatton, Y. Mengüç, Soft Snake Robots: Mechanical design and geometric gait implementation, in *2017 IEEE International Conference on Robotics and Biomimetics (ROBIO)* (IEEE, 2017), pp. 282–289.
- X. Qi, T. Gao, X. Tan, Bioinspired 3D-printed snakeskins enable effective serpentine locomotion of a soft robotic Snake. *Soft Robot.* **10**, 568–579 (2023).
- M. Yim, Y. Zhang, D. Duff, Modular robots. *IEEE Spectr.* **39**, 30–34 (2002).
- X. Wu, S. Ma, Cpg-based control of serpentine locomotion of a snake-like robot. *Mechatronics* **20**, 326–334 (2010).
- Q. Fu, C. Li, Robotic modelling of snake traversing large, smooth obstacles reveals stability benefits of body compliance. *R. Soc. Open Sci.* **7**, 191192 (2020).
- T. Takemori, M. Tanaka, F. Matsuno, Adaptive helical rolling of a snake robot to a straight pipe with irregular cross-sectional shape. *IEEE Trans. Robot.* **39**, 437–451 (2023).
- P. E. Schiebel, M. C. Maisonneuve, K. Diaz, J. M. Rieser, D. I. Goldman, Robophysical modeling of bilaterally activated and soft limbless locomotors, in V. Vouloutsis, A. Mura, F. Tauber, T. Speck, T. J. Prescott, P. F. M. J. Verschuer, Eds. *Biomimetic and Biohybrid Systems. Living Machines 2020. Lecture Notes in Computer Science* (Springer, 2020), pp. 300–311.
- J. H. Boyle, S. Johnson, A. A. Dehghani-Sanj, Adaptive undulatory locomotion of a *C. elegans* inspired robot. *IEEE/ASME Trans. Mechatron.* **18**, 439 (2012).
- P. Racioppo, M. Ben-Tzvi, Design and control of a cable-driven articulated modular snake robot. *IEEE ASME Trans. Mechatron.* **24**, 893–901 (2019).
- B. Webb, Can robots make good models of biological behaviour? *Behav. Brain Sci.* **24**, 1033–1050 (2001).
- Y. O. Aydin, J. M. Rieser, C. M. Hubicki, W. Savoie, D. I. Goldman, Physics approaches to natural locomotion: Every robot is an experiment. *Robot. Syst. Auton. Platforms*, 109–127 (2019).
- L. R. Varshney, B. L. Chen, E. Paniagua, D. H. Hall, D. B. Chklovskii, Structural properties of the *Caenorhabditis elegans* neuronal network. *PLOS Comput. Biol.* **7**, e1001066 (2011).
- C. Fang-Yen, M. J. Alkema, A. D. Samuel, Illuminating neural circuits and behaviour in *Caenorhabditis elegans* with optogenetics. *Philos. Trans. R. Soc. Lond. B Biol. Sci.* **370**, 20140212 (2015).
- J. P. Nguyen, F. B. Shipley, A. N. Linder, G. S. Plummer, M. Liu, S. U. Setru, J. W. Shaevitz, A. M. Leifer, Whole-brain calcium imaging with cellular resolution in freely behaving *Caenorhabditis elegans*. *Proc. Natl. Acad. Sci. U. S. A.* **113**, E1074–E1081 (2016).
- S. Park, H. Hwang, S. W. Nam, F. Martinez, R. H. Austin, W. S. Ryu, Enhanced *Caenorhabditis elegans* locomotion in a structured microfluidic environment. *PLOS ONE* **3**, e2550 (2008).
- T. Majumdar, E. E. Keaveny, J. Zhang, M. J. Shelley, Experiments and theory of undulatory locomotion in a simple structured medium. *J. R. Soc. Interface* **9**, 1809–1823 (2012).

56. J. M. Rieser, C. Gong, H. C. Astley, P. E. Schiebel, R. L. Hatton, H. Choset, D. I. Goldman, Geometric phase and dimensionality reduction in locomoting living systems. *arXiv:1906.11374* [physics.bio-ph] (2019); <https://doi.org/10.48550/arXiv.1906.11374>.
57. B. Chong, T. Wang, E. Erickson, P. J. Bergmann, D. I. Goldman, Coordinating tiny limbs and long bodies: Geometric mechanics of lizard terrestrial swimming. *Proc. Natl. Acad. Sci. U. S. A.* **119**, e2118456119 (2022).
58. G. J. Stephens, B. Johnson-Kerner, W. Bialek, W. S. Ryu, Dimensionality and dynamics in the behavior of *C. elegans*. *PLOS Comput. Biol.* **4**, e1000028 (2008).
59. J. Sznitman, X. Shen, R. Sznitman, P. E. Arratia, Propulsive force measurements and flow behavior of undulatory swimmers at low Reynolds number. *Phys. Fluids* **22**, 121901 (2010).
60. T. Zhang, D. I. Goldman, The effectiveness of resistive force theory in granular locomotion. *Phys. Fluids* **26**, 101308 (2014).
61. J. Gray, G. Hancock, The propulsion of sea-urchin spermatozoa. *J. Exp. Biol.* **32**, 802–814 (1955).
62. S. Hirose. *Biologically Inspired Robots: Snake-Like Locomotors and Manipulators* (Oxford Univ. Press, 1993).
63. B. Zhao, P. Khare, L. Feldman, J. A. Dent, Reversal frequency in *Caenorhabditis elegans* represents an integrated response to the state of the animal and its environment. *J. Neurosci.* **23**, 5319–5328 (2003).
64. D. B. Doroquez, C. Berciu, J. R. Anderson, P. Sengupta, D. Nicastro, A high-resolution morphological and ultrastructural map of anterior sensory cilia and glia in *Caenorhabditis elegans*. *eLife* **3**, e01948 (2014).
65. M. Chatzigeorgiou, W. R. Schafer, Lateral facilitation between primary mechanosensory neurons controls nose touch perception in *C. elegans*. *Neuron* **70**, 299–309 (2011).
66. H. Hauser, A. J. Ijspeert, R. M. Fölschlin, R. Pfeifer, W. Maass, Towards a theoretical foundation for morphological computation with compliant bodies. *Biol. Cybern.* **105**, 355–370 (2011).
67. C. Laschi, B. Mazzolai, Lessons from animals and plants: The symbiosis of morphological computation and soft robotics. *IEEE Robot. Autom. Mag.* **23**, 107–114 (2016).
68. T. Kano, A. Ishiguro, Obstacles are beneficial to me! Scaffold-based locomotion of a snake-like robot using decentralized control, in *2013 IEEE/RSJ International Conference on Intelligent Robots and Systems (IROS)* (IEEE, 2013), pp. 3273–3278.
69. M. Travers, J. Whitman, P. Schiebel, D. Goldman, H. Choset, Shape-based compliance in locomotion. *Robot. Sci. Syst.* **12** (2016).
70. G. Sartoretto, T. Wang, G. Chuang, Q. Li, H. Choset, Autonomous decentralized shape-based navigation for snake robots in dense environments, in *2021 IEEE International Conference on Robotics and Automation (ICRA)* (IEEE, 2021), pp. 9276–9282.
71. Z. Bing, C. Lemke, F. O. Morin, Z. Jiang, L. Cheng, K. Huang, A. Knoll, Perception-action coupling target tracking control for a snake robot via reinforcement learning. *Front. Neurobot.* **14**, 591128 (2020).
72. K. G. Hanssen, A. A. Transteth, F. Sanfilippo, P. Liljebäck, Ø. Stavadahl, Path planning for perception-driven obstacle-aided snake robot locomotion, in *2020 IEEE 16th International Workshop on Advanced Motion Control (AMC)* (IEEE, 2020), pp. 98–104.
73. R. D. Maladen, Y. Ding, P. B. Umbanhowar, D. I. Goldman, Undulatory swimming in sand: Experimental and simulation studies of a robotic sandfish. *Int. J. Rob. Res.* **30**, 793–805 (2011).
74. B. Chong, T. Wang, D. Irvine, V. Kojouharov, B. Lin, H. Choset, D. I. Goldman, G. Blekherman, Gait design for limbless obstacle aided locomotion using geometric mechanics. *Robotics: Science and Systems* (2023).
75. J. H. Long Jr., Muscles, elastic energy, and the dynamics of body stiffness in swimming eels. *Am. Zool.* **38**, 771–792 (1998).
76. M. Backholm, W. S. Ryu, K. Dalnoki-Veress, Viscoelastic properties of the nematode *Caenorhabditis elegans*, a self-similar, shear-thinning worm. *Proc. Natl. Acad. Sci. U. S. A.* **110**, 4528–4533 (2013).
77. M. Gazzola, M. Argentina, L. Mahadevan, Gait and speed selection in slender inertial swimmers. *Proc. Natl. Acad. Sci. U. S. A.* **112**, 3874–3879 (2015).
78. J. H. Boyle, S. Berri, N. Cohen, Gait modulation in *C. elegans*: An integrated neuromechanical model. *Front. Comput. Neurosci.* **6**, 10 (2012).
79. J. E. Denham, T. Ranner, N. Cohen, Signatures of proprioceptive control in *Caenorhabditis elegans* locomotion. *Philos. Trans. R. Soc. Lond. B Biol. Sci.* **373**, 20180208 (2018).
80. G. Haspel, K. E. Severi, L. J. Fauci, N. Cohen, E. D. Tytell, J. R. Morgan, Resilience of neural networks for locomotion. *J. Physiol.* **599**, 3825–3840 (2021).
81. T. Wang, B. Chong, Y. Deng, R. Fu, H. Choset, D. I. Goldman, Generalized omega turn gait enables agile limbless robot turning in complex environments, in *2022 International Conference on Robotics and Automation (ICRA)* (IEEE, 2022), pp. 1–7.
82. B. Chong, T. Wang, J. M. Rieser, B. Lin, A. Kaba, G. Blekherman, H. Choset, D. I. Goldman, Frequency modulation of body waves to improve performance of sidewinding robots. *Int. J. Rob. Res.* **40**, 1547–1562 (2021).
83. A. J. Ijspeert, Central pattern generators for locomotion control in animals and robots: A review. *Neural Netw.* **21**, 642–653 (2008).
84. R. Thandiackal, K. Melo, L. Paez, J. Herault, T. Kano, K. Akiyama, F. Boyer, D. Ryczko, A. Ishiguro, A. J. Ijspeert, Emergence of robust self-organized undulatory swimming based on local hydrodynamic force sensing. *Sci. Robot.* **6**, eabf6354 (2021).
85. G. Bellegarda, A. Ijspeert, Cpg-rl: Learning central pattern generators for quadruped locomotion. *IEEE Robot. Autom. Lett.* **7**, 12547–12554 (2022).
86. T. Haarnoja, H. Tang, P. Abbeel, S. Levine, Reinforcement learning with deep energy-based policies, in *International Conference on Machine Learning (PMLR, 2017)*, pp. 1352–1361.
87. S. Ramasamy, R. L. Hatton, Optimal gaits for drag-dominated swimmers with passive elastic joints. *Phys. Rev. E* **103**, 032605 (2021).
88. G. Strang, *Introduction to Linear Algebra*, Vol. 3 (Wellesley-Cambridge Press, 1993).
89. J. M. Rieser, P. E. Schiebel, A. Pazouki, F. Qian, Z. Goddard, K. Wiesenfeld, A. Zangwill, D. Negrut, D. I. Goldman, Dynamics of scattering in undulatory active collisions. *Phys. Rev. E* **99**, 022606 (2019).
90. S. Alben, Efficient sliding locomotion with isotropic friction. *Phys. Rev. E* **99**, 062402 (2019).
91. Z. Altun, D. H. Hall, Muscle system, somatic muscle. In *WormAtlas* (2009). doi:10.3908/wormatlas.1.7.
92. H. C. Berg, *Random Walks in Biology* (Princeton Univ. Press, 1993).
93. G. Gabrielli, What price speed? *Mech. Eng.* **72**, 775 (1950).
94. S. Seok, A. Wang, M. Y. Chuah, D. Otten, J. Lang, S. Kim, Design principles for highly efficient quadrupeds and implementation on the MIT Cheetah robot, in *2013 IEEE International Conference on Robotics and Automation (IEEE, 2013)*, pp. 3307–3312.
95. U. Saranli, M. Buehler, D. E. Koditschek, RHex: A simple and highly mobile hexapod robot. *Int. J. Robot. Res.* **20**, 616–631 (2001).
96. R. L. Hatton, Y. Ding, H. Choset, D. I. Goldman, Geometric visualization of self-propulsion in a complex medium. *Phys. Rev. Lett.* **110**, 078101 (2013).
97. A. Parashar, R. Lycke, J. A. Carr, S. Pandey, Amplitude-modulated sinusoidal microchannels for observing adaptability in *C. elegans* locomotion. *Biomicrofluidics* **5**, 024112 (2011).
98. J. Yuan, D. M. Raizen, H. H. Bau, Gait synchronization in *Caenorhabditis elegans*. *Proc. Natl. Acad. Sci. U. S. A.* **111**, 6865–6870 (2014).

Acknowledgments: We thank Z. Shen for the help with manufacturing the head collision sensor; D. Soto for the help with construction of robophysical experiment environment; V. Zborovsky for the help with robophysical (indoor) experiments; Z. Xu, A. Bhumkar, and N. Mankame for their help with robophysical (outdoor) experiments; Z. James for the help with biological experiments; and L. Peng for useful discussions. **Funding:** This work was supported by the Army Research Office Grant (W911NF-11-1-0514), National Science Foundation Physics of Living Systems Student Research Network (GR10003305), NSF-Simons Southeast Center for Mathematics and Biology (National Science Foundation DMS1764406, Simons Foundation SFARI 594594), and the Dunn Family Professorship. **Author contributions:** Conceptualization: T.W., C.P., V.K., and D.I.G. Methodology: T.W., C.P., V.K., B.C., and K.D. Investigation: T.W., C.P., V.K., B.C., and K.D. Visualization: T.W. and C.P. Funding acquisition: D.I.G. and H.L. Project administration: D.I.G. and H.L. Supervision: D.I.G. and H.L. Writing—original draft: T.W., C.P., and D.I.G. Writing—review and editing: T.W., C.P., V.K., B.C., K.D., H.L., and D.I.G. **Competing interests:** Some of the subject matter herein may be implicated in one or more pending patent applications such as PCT Patent Application no. PCT/US2022/043362, titled “Devices and systems for locomoting diverse terrain and methods of use,” which claims the benefit of priority to US Provisional App. no. 63/243,435 filed on 13 September 2021, and US Provisional App. no. 63/318,868 filed on 11 March 2022. The authors declare that they have no other competing interests. **Data and materials availability:** All data are available in the main text or the Supplementary Materials.

Submitted 11 April 2023
 Accepted 28 November 2023
 Published 20 December 2023
 10.1126/scirobotics.adi2243